Article

Determining the Orbital Angular Momentum of a Vortex Beam Using Strong Field Ionization

Harrison Pasquinilli, Alex Schimmoller, Spencer Walker ![ORCID] and Alexandra S. Landsman *

Department of Physics, The Ohio State University, Columbus, OH 43210, USA; pasquinilli.3@buckeyemail.osu.edu (H.P.); schimmoller.11@osu.edu (A.S.); walker.2190@osu.edu (S.W.)
* Correspondence: landsman.7@osu.edu

Abstract: While interferometric methods exist for classifying vortex states of light, these techniques usually require destroying the beam of interest to determine the light's OAM. A recent two-color pump-probe experiment employed strong field ionization and beam sculpting to classify vortex beams. Here, we propose an alternative strong-field method for distinguishing OAM states of light which does not require beam sculpting and instead utilizes a noncollinear terahertz standing wave to probe ionized electrons. We then use classical trajectory Monte Carlo (CTMC) methods to simulate strong-field ionization of helium under this configuration with the terahertz field both on and off. We find that the resulting electron momenta distributions can be used to extract the OAM of the beam, as long as the vortex beam spot size does not exceed 1/4 the terahertz pulse's wavelength.

Keywords: orbital angular momentum of light; vortex optics; strong-field ionization

1. Introduction

The total angular momentum, **j**, of a photon consists of an orbital angular momentum (OAM) component, **l**, which describes the spatial distribution of the photon field and an intrinsic spin angular momentum (SAM) component, **s**, that is related to the polarization of the field [1–3]. One of the simplest problems discussed in the study of light–matter interaction involves striking a target with monochromatic circularly polarized plane-wave radiation [4,5]. In this situation, photons contain a single unit of spin angular momentum $\pm\hbar$ due to the field polarization where $\hbar$ denotes the reduced Planck constant. In contrast, application of $\hat{L}_z = -i\hbar\frac{\partial}{\partial\phi}$ to the scalar plane-wave component $\exp(i\mathbf{k}\cdot\mathbf{r})$ shows that plane-wave fields contain no orbital angular momentum. The expansion of this field in OAM components

$$\exp(i\mathbf{k}\cdot\mathbf{r}) = \exp(ik_z z)\sum_{\ell=-\infty}^{\infty}(i)^{\ell}J_{\ell}(k_r r)\exp\left[i\ell(\phi-\phi_k)\right] \tag{1}$$

around the quantization axis $\hat{\mathbf{z}}$ [6] shows that the field contains all integral orbital momentum components $\hbar\ell = \cdots, -\hbar, 0, \hbar, 2\hbar, \cdots$ and only averages to zero once the expectation value is taken. These components themselves are cylindrical solutions to the wave equation and therefore describe physical states containing OAM $\hbar\ell$ [7]. Here r and ϕ describe the cylindrical distance and angle perpendicular to the quantization axis, J_{ℓ} are the cylindrical Bessel functions and k_r, k_z and ϕ_k parameterize the wave-vector **k** in cylindrical coordinates. Taking $r \to 0$, it is clear that all momentum components satisfying $\ell \neq 0$ vanish. Loops taken around such singularities accumulate a phase $2\pi\ell$ where ℓ is often referred to as a topological charge [8,9].

In the past 30 years [3,10–12], there has been growing interest in vortex optics within a diverse range of applications spanning from astronomy [13–15] to particle manipulation [16–18] and communication [19,20]. In particular, these fields have generated great excitement in quantum and semi-classical optics where strong field gradients

near vortex centers have caused observed breakdown of the dipole selection rules and open a new path for exploration and control of light–matter interactions [7,21–24]. There has also been a growing interest in singular optics in the strong-field regime. High-order harmonics carrying orbital angular momentum have been experimentally generated [25–28] and studied theoretically [29,30] with the overall goal of creating light pulses with controllable OAM values. Studies of strong-field ionization have been limited to experiments involving Argon gas [31] and theoretical quantum trajectory Monte Carlo simulations of SFI involving Bessel beams [32]. Accurate descriptions of these fields are required in order to have maximum impact in each of these applications. Ongoing investigations include using interferometric techniques [13,33], autocorrelation methods [34], and reconstructions based on triangular apertures [35] to determine OAM.

Recently, a noteworthy non-destructive method has been demonstrated for the determination of the OAM of photons contained within a circularly polarized femtosecond pulse at 400 nm [36]. This two-color pump-probe ionization scheme uses the aforementioned 400 nm vortex field to be characterized and an additional co-rotating circularly polarized plane-wave field at 800 nm. In this method, the OAM ℓ is determined via a two-color phase structure imprinted on the angle-resolved photo-electron momentum distribution after ionization. This method shows great success differentiating pulses containing either $\ell = 0$ or $\ell \neq 0$ OAM, but requires pulse sculpting to determine the particular value of $\ell \neq 0$.

In this article, we perform a theoretical study of atomic helium's interaction with an intense vortex field. We find that photo-electron momentum distributions generated from classical trajectory Monte Carlo simulations exhibit local carrier envelope phase effects depending on where the electron is ionized with respect to the vortex center, allowing one to distinguish between ionization from vortex and non-vortex light with circular polarization, but not different vortex states. We then propose a new technique for experimentally distinguishing between different vortex states of light using strong-field ionization. Within this scheme, a linearly polarized infrared vortex beam is probed by a low frequency terahertz field. The probing pulse in this two-color method manifests itself as a linearly polarized terahertz standing plane-wave field with orthogonal polarization to the vortex beam, as shown in Figure 1. Spatial information is imprinted upon ionized photo-electrons and can be used to extract the OAM, provided that the vortex beam spot size is sufficiently small relative to the probing field wavelength. Monte Carlo simulations utilizing a 245 μm probing field are applied to theoretically confirm the method for vortex beams at 800 nm containing OAM $|\ell| = 0, \cdots, 8$.
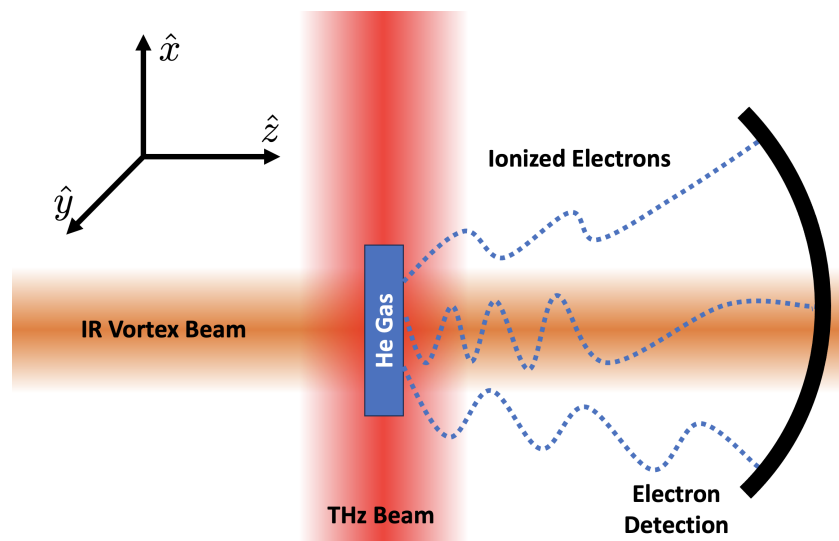

Figure 1. Schematic view of the proposed experimental set-up. The infrared vortex beam of Equation (2) to be characterized is polarized in the $\hat{x}$ direction and propagates along the $\hat{z}$ axis. The pulse strikes a

helium gas sample at its focus ($z = 0$) and triggers ionization. An additional terahertz standing wave (Equation (4)) propagating along the $\hat{\mathbf{x}}$-axis irradiates the sample and imprints extra momentum onto ionized electrons along its polarization axis $\hat{\mathbf{y}}$. The value of this additional momentum changes depending on the location of the atom to be ionized relative to the vortex center and allows for the determination of OAM.

2. Methods

This study consists of two primary sections: first, an analysis of atomic strong field ionization by a vortex field alone. We then take advantage of the fundamental properties of strong field ionization and vortex optics to propose a scheme for systematically differentiating vortex beams with different OAM values. This section details the theoretical models used to simulate the light pulses, as well as the photo-electron ionization and propagation steps.

2.1. Modeling the Vortex and Terahertz Fields

The Laguerre–Gaussian modes are vortex states of light which exactly solve Maxwell's wave equation in vacuum restricted to the paraxial limit. Suppose that an intense field of linearly-polarized infrared light is prepared in a Laguerre–Gaussian state with radial index $p = 0$ and OAM magnitude $|\ell| \geq 0$. The electric field of such a Laguerre–Gaussian beam with central (angular) frequency ω restricted to the plane of the beam focus ($z = 0$) is given by [37].

$$
\begin{aligned}
\mathbf{E}_\ell(\mathbf{r}, t) = & E_{\mathrm{LG}} \frac{|\ell|^{-|\ell|/2}}{\sqrt{1 + \epsilon^2}} e^{i(\omega t + l\phi)} [\hat{\mathbf{x}} - i\epsilon\hat{\mathbf{y}}] \\
& \times \left[\frac{\sqrt{2}r}{w_0} \right]^{|\ell|} \exp\left(\frac{|\ell|}{2} - \frac{r^2}{w_0^2} \right) \mathrm{env}_{\mathrm{LG}}(t),
\end{aligned}
\tag{2}
$$

where $\{r, \phi, z\}$ are the 3D cylindrical coordinates, E_{LG} is the pulse's maximum electric field (normalized by the $|\ell|^{-|\ell|/2} e^{|\ell|/2}$ term), ϵ is the pulse's ellipticity, w_0 is the beam waist radius and $\mathrm{env}_{\mathrm{LG}}(t) = \cos^2\left(\frac{\omega t}{2N}\right)$ is the envelope function which lasts for N cycles and determines pulse duration. The index $\ell = 0, \pm 1, \pm 2, \ldots$ determines the orbital angular momentum value of the beam. In the limit where $\ell = 0$, the equation for a Gaussian beam in the plane of focus is recovered. When $\ell \neq 0$, the beam takes on a phase singularity at the origin, reaching maximum intensity in a ring surrounding the singularity. See Figure 2 for intensity and phase profiles for $\ell = 0$ and $\ell = 1$ beams. According to the Ammosov–Delone–Krainov (ADK) theory [38], the probability for ionization by an intense electric field is most likely near the field peak and is exponentially suppressed otherwise. For Gaussian beams, this peak occurs at the beam's spatial focus and temporal center, i.e., $\mathbf{r} = t = 0$. However, for cylindrically symmetric beams such as the LG modes, the intensity peak occurs at a ring surrounding the singularity in the $z = 0$ plane. The radius of this peak, based on Equation (2), is given by

$$
r_{\mathrm{peak}} = w_0 \sqrt{\frac{|\ell|}{2}}.
\tag{3}
$$

Hence, for a given beam waist radius w_0, the radial peak of a vortex beam is proportional to the square root of $|\ell|$. Therefore, keeping all other beam parameters constant, increasing the orbital index corresponds to increasing the radius of the vortex beam.

In order to map electrons' ionization locations onto their momenta, we introduce a noncollinear terahertz standing wave which is linearly polarized in a direction transverse to the OAM field primary axis:

$$\mathbf{E}_{\mathrm{THz}}(\mathbf{r}, t) = E_{\mathrm{THz}} \cos(\omega_{\mathrm{THz}} t) \sin(kx) \mathrm{env}_{\mathrm{THz}}(t) \hat{\mathbf{y}}, \tag{4}$$

where E_{THz}, ω_{THz} and k are the terahertz field magnitude, frequency and wave number, respectively, and $\mathrm{env}_{\mathrm{THz}}(t) = \cos^2\left(\frac{\omega_{\mathrm{THz}} t}{2N^I}\right)$ is the enveloping function for the probe pulse lasting N^I cycles. This field exhibits a node at the vortex singularity ($x = 0$) and grows in amplitude as one moves away from the vortex center. To better understand the simulation geometry, see Figures 1 and 3.
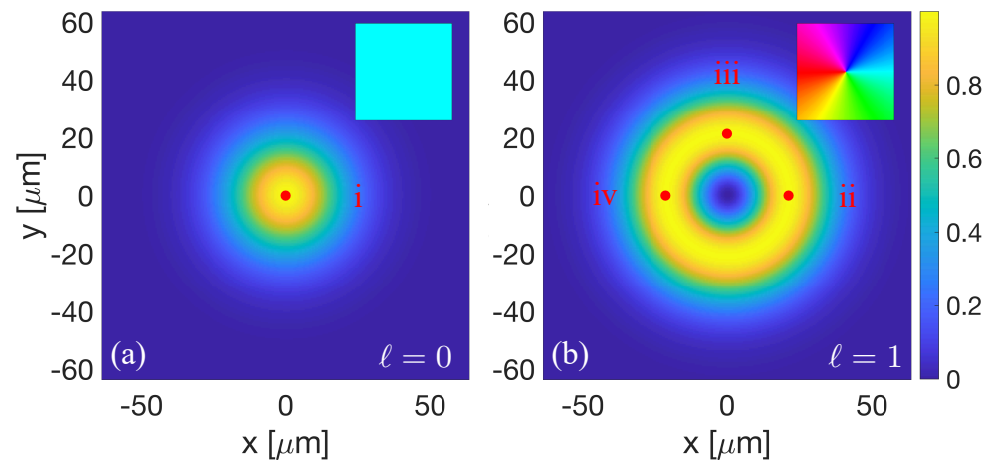

Figure 2. Intensity profiles for non-vortex (**a**) and vortex (**b**) beams. (**a**) Gaussian beam with beam waist $w_0 = 30$ microns. (**b**) Laguerre–Gaussian beam with the same beam waist and $\ell = 1$. Insets show the accompanying phase profiles for each beam. Red dots (i–iv) indicate points of interest for simulations. The intensity color mapping is normalized to the peak of the electric field.
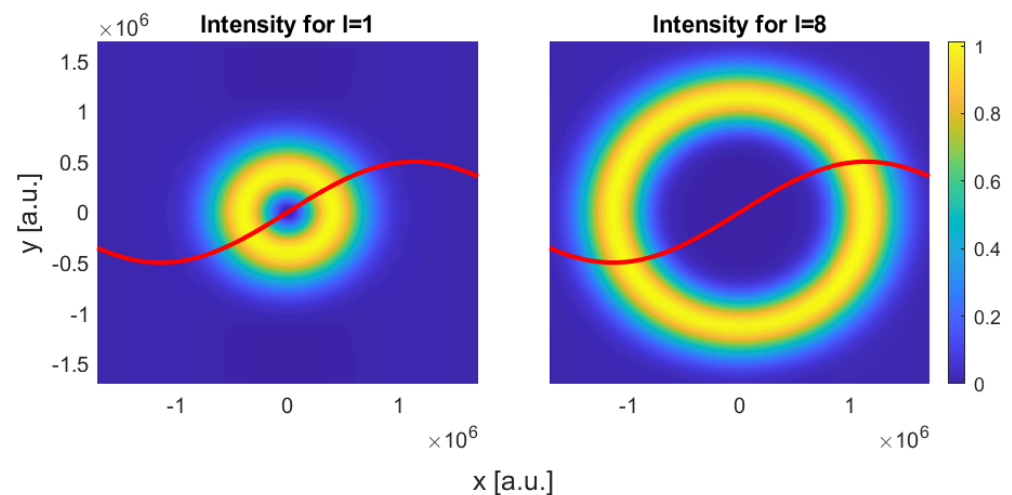

Figure 3. A combined field profile of the two beams in the x-y plane at $\ell = 1$ (**left**), and $\ell = 8$ (**right**). The color plot depicts the field intensity profile normalized to the peak of the LG beam. Overlaid on both beams is the field profile in x of the THz beam. The spatial profile is properly depicted, and the amplitude is displayed in arbitrary units.

2.2. Classical Trajectory Monte Carlo Simulations

Within the combined field

$$\mathbf{E}_{\mathrm{total}}(\mathbf{r}, t) = \mathrm{Re}\{\mathbf{E}_\ell(\mathbf{r}, t)\} + \mathbf{E}_{\mathrm{THz}}(\mathbf{r}, t), \tag{5}$$

where Re$\{\cdot\}$ designates the real part of the input, electrons ionized by the strong vortex infrared field receive additional $\hat{\mathbf{y}}$ momentum from the weak THz probe pulse. The amount of this additional momentum increases as one approaches the standing wave peak of the THz field. Assuming the laser pulses to be finite and for the electron excursion to be much smaller than the spatial variation of the beams, conservation of canonical momentum states that the electron momenta $\mathbf{p}_i$ at the time of ionization t_0 and momenta $\mathbf{p}_f$ after the pulses end are related by

$$\mathbf{p}_f = \mathbf{p}_i - \mathbf{A}_{\text{total}}(\mathbf{r}_{\text{atom}}, t_0), \tag{6}$$

where the vector potential is determined by the electric field (Equation (5)) and given by $\mathbf{E}_{\text{total}}(\mathbf{r}, t) = -\frac{\partial}{\partial t}\mathbf{A}_{\text{total}}(\mathbf{r}, t)$, where the field is assumed to be locally uniform in space. (Note that we have neglected the Coulomb interaction between the parent ion and the ionized electron, which has a relatively small effect on the electron trajectory [39]). Therefore, the presence of the probe field (Equation (4)) leads to an additional spread in the electron's $\hat{\mathbf{y}}$ momentum, which can be detected and allow for differentiation between different OAM values of the ionizing vortex beam.

2.3. Monte Carlo Simulations

We employ classical trajectory Monte Carlo simulations (CTMC) to model the proposed set-up shown in Figures 1 and 3. Consider helium atoms (ionization energy $I_{p,0}$ = 24.59 eV) which are uniformly distributed in the x-y plane with z = 0. These atoms may be ionized by the combined laser electric field (Equation (5)), with the ionization rate given by the ADK theory [38]:

$$P(\mathbf{r}_{\text{atom}}, v_\perp, t) \propto \exp\left(-\frac{2}{3}\frac{[2I_p(t)]^{\frac{3}{2}}}{|\mathbf{E}_{\text{total}}(\mathbf{r}_{\text{atom}}, t)|} - v_\perp^2\frac{\sqrt{2I_p(t)}}{|\mathbf{E}_{\text{total}}(\mathbf{r}_{\text{atom}}, t)|}\right), \tag{7}$$

where $\mathbf{r}_{\text{atom}} = (r, \phi, z = 0)$ is the atom's position, $v_\perp$ is the electron's initial speed transverse to the instantaneous electric field after ionization, and the Stark-shifted ionization energy $I_p(t)$ is given by

$$I_p(t) = I_{p,0} + \frac{1}{2}(\alpha_N - \alpha_I)|\mathbf{E}_{\text{total}}(\mathbf{r}_{\text{atom}}, t)|^2, \tag{8}$$

where α_N = 1.38 a.u. and α_I = 9/32 a.u. are the polarizabilities of the atom and ion, respectively. Hartree atomic units ($e = m_e = \hbar = 1$ a.u.) are used throughout unless specified otherwise. The LG beam (Equation (2)) has a peak intensity of $2 \cdot 10^{14}$ W/cm^2, wavelength of λ = 800 nm, and beam waist radius of 30 μm. The envelope for this pulse is restricted to N = 8 cycles. Meanwhile, the perturbing terahertz beam (Equation (4)) has a peak intensity of $3 \cdot 10^{12}$ W/cm^2 similar to that in [40], as well as a wavelength of λ = 245 μm, and is also limited to $N' = 8$ cycles. These laser parameters are chosen so as to satisfy the following relevant conditions:

- The vortex field is strong enough to tunnel ionize the sample. That is, its peak intensity $|E_{\text{LG}}|^2 \lesssim 1$ atomic unit and $\omega \ll I_p$.
- The terahertz field is too weak to significantly change the ionization yields. In other words, the vortex field dominates during ionization. Therefore, $|E_{\text{THz}}|^2 \ll |E_{\text{LG}}|^2$.
- The terahertz field is strong enough to alter the variation in y-momentum. This condition implies the terahertz field ponderomotive energy far exceeds the photoelectron momentum standard deviation present in the ADK ionization rate (7):

$$\frac{|E_{\text{THz}}|^2}{4\omega_{\text{THz}}^2} \gg \left(\frac{|E_{\text{LG}}|}{2\sqrt{2I_{p,0}}}\right)^{1/2}. \tag{9}$$

- Each of the pulses is sufficiently long to employ analytical models which assume plane wave radiation, such as the ADK model [38].
- The terahertz wavelength exceeds the Laguerre–Gaussian pulse's waist radius. More on this point is stated in the Results and Discussion sections.

We perform Monte Carlo reject sampling based on the ionization rate (Equation (7)) by sampling over a random distribution of ionization times t_0, transverse velocities $v_\perp$, and atom locations $\mathbf{r}_{atom}$ in order to achieve ionization times and initial momenta for electron trajectories. Initial positions $\mathbf{r}_0$ for these electrons are then determined using the tunnel ionization in parabolic coordinates with induced dipole and Stark shift (TIPIS) model [41]:

$$|\mathbf{r}_0 - \mathbf{r}_{atom}| = \frac{I_p(t_0) + \sqrt{I_p(t_0)^2 + 4\beta|\mathbf{E}_{total}(t_0, \mathbf{r}_{atom})|}}{2|\mathbf{E}_{total}(t_0, \mathbf{r}_{atom})|}, \tag{10}$$

where

$$\beta = 1 - \frac{\sqrt{2I_p(t_0)}}{2}. \tag{11}$$

The direction of the tunnel exit at a particular ionization time and atomic location is opposite the instantaneous electric field. Ionized electrons then propagate as classical particles obeying Newton's equation,

$$\ddot{\mathbf{r}} = -\mathbf{E}_{total}(\mathbf{r}, t), \tag{12}$$

where liberated electrons interact with the spatially varying field (Equation (5)) until the end of both laser pulses, and the atomic Coulomb force is neglected. Simulations are performed with 10^5 electron trajectories, and final electron momenta are recorded. We repeat the calculations for various vortex beam OAM values, allowing for comparison.

3. Results

3.1. Vortex Beam Strong-Field Ionization

To begin, we consider the case where the atomic sample interacts with the Laguerre–Gaussian pump only and set $\mathbf{E}_{THz} = 0$. Atoms are confined to points of maximum intensity within each beam profile indicated in Figure 2, allowing us to compare and contrast electron momenta for electrons ionized by vortex and non-vortex beams. Results can be seen in Figures 4 and 5 for circular ($\epsilon = 1$) and linear light ($\epsilon = 0$), respectively.

In the case of circular polarization (Figure 4), electrons create a momentum ring of radius E_ℓ/ω in the $v_x - v_y$ plane no matter the ionization location or ℓ value. This can be understood through the conservation of canonical momentum (Equation (6)): When $\epsilon = 1$, an electron ionized at time t_0 experiences an electric field $\mathbf{E}_l(\mathbf{r}_{atom}, t_0)$. The corresponding vector potential $\mathbf{A}_l \perp \mathbf{E}_l$. Since the field magnitude is roughly constant around the peak of the envelope while the field direction rotates in space, according to Equation (6), photo-electrons trace out a ring with radius roughly equal to the maximum vector potential, E_ℓ/ω.

Looking more closely, one sees that each momentum ring in Figure 4 displays a well-defined peak displayed in dark red corresponding to electrons ionized near the exact peak of the pulse envelope. However, the location of this peak on the momentum ring varies depending on the ionization location. This can be interpreted as a consequence of the local carrier envelope phase (CEP) introduced by the vortex beam: Recall that the vortex field (2) contains a spiraling phase profile around the beam propagation direction, i.e., in the x-y plane. In effect, this rotates the polarization direction of the pulse peak depending on the azimuthal phase of the ionization location $\mathbf{r}_{atom}$, and therefore also shifts the vector potential direction and peak in electron momentum.
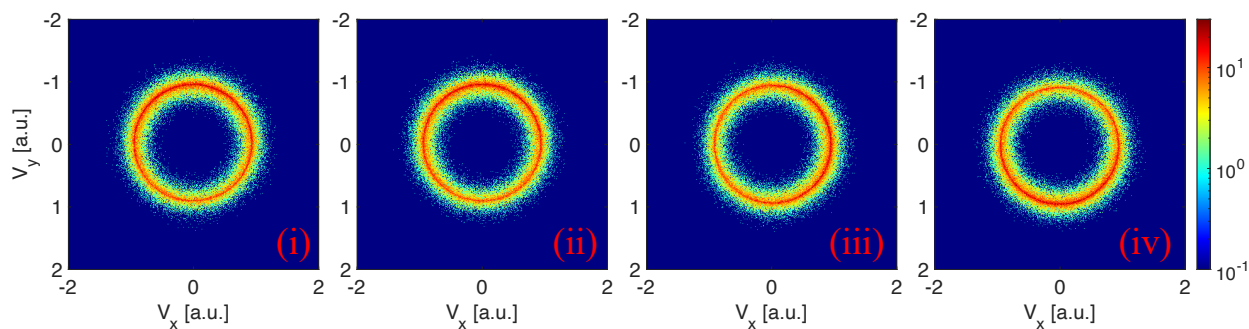
Figure 4. Photo-electron momentum distributions (PMDs) resulting from strong field ionization by circularly polarized laser pulses. Figure indexing (**i**–**iv**) corresponds to the ionization locations and beam profiles depicted in Figure 2.
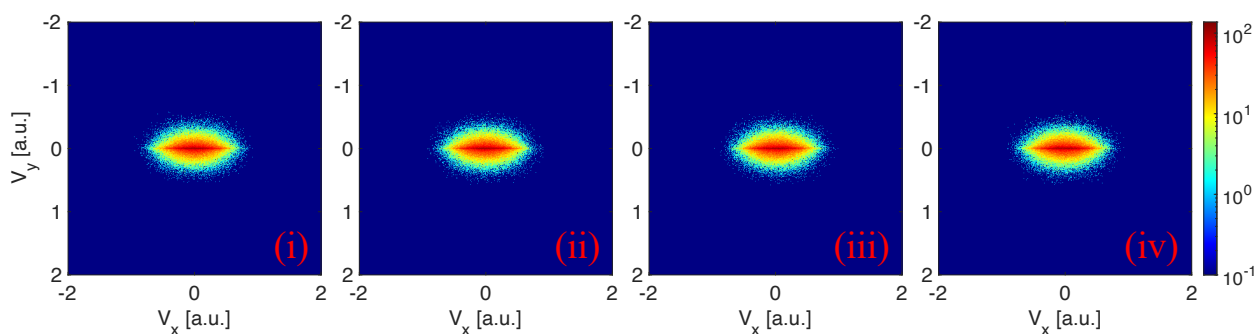

Figure 5. Photo-electron momentum distributions (PMDs) resulting from strong field ionization by linearly polarized laser pulses. Figure indexing (**i**–**iv**) corresponds to the ionization locations and beam profiles depicted in Figure 2.

Observing a similar effect for linearly polarized light is more difficult. When $\epsilon = 0$ (see Figure 5), the vector potential is minimized at the peak of the electric field. Carrier envelope phase effects are much harder to observe for linearly polarized light compared to circular, making photo-electron momenta from Laguerre–Gaussian beams of different ℓ values indistinguishable.

We also perform CTMC simulations with the atomic position $\mathbf{r}_{\text{atom}}$ treated as an additional random variable within the reject-sampling algorithm. Results can be seen in Figure 6: it appears that the Gaussian beam ($\ell = 0$) creates photo-electrons which maintain a well-defined momentum peak, whereas the vortex fields introduce CEP averaging and eliminate any bias in the electron momenta direction. Therefore, these simulations allow for clear distinguishing between vortex and non-vortex states, but not between beams of different ℓ values. This is in agreement with experimental results in reference [36], Figure 2.
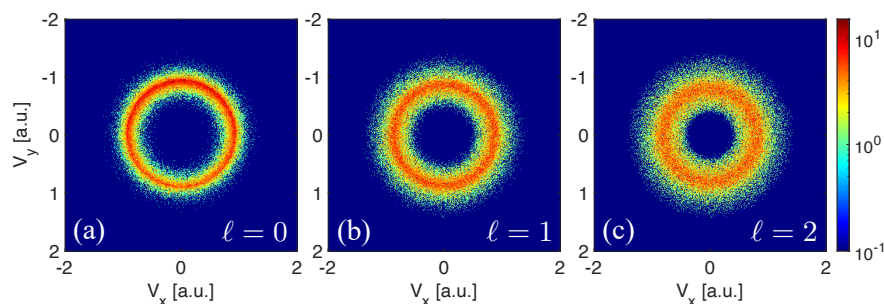

Figure 6. Photo-electron momentum distributions (PMDs) resulting from strong field ionization by (**a**) Gaussian and (**b**,**c**) Laguerre–Gaussian circularly polarized laser pulses. Here, electrons may be ionized from anywhere within the $\hat{x}$-$\hat{y}$ plane.

3.2. Distinguishing OAM States of Light Using a Terahertz Probe Pulse

Distinguishing between Laguerre–Gaussian beams with different $|\ell|$ magnitudes is made possible by turning on the terahertz probe pulse. Here, we perform the same CTMC simulations with linearly polarized light, this time with the full $\mathbf{E}_{\text{total}}$ profile (5). The simulation results are summarized within Figure 7: Here (panel b), the standard deviation in photo-electron $\hat{\mathbf{y}}$ momentum is plotted as a function of the vortex beam OAM value ℓ, with simulations performed with approximate, spatially uniform (blue) and accurate, spatially varying (red) electric fields. In the former, after initial conditions are generated, final electron momenta can be calculated from Equation (6), whereas the latter are determined by numerically solving Newton's equation (12). While accounting for the spatially varying electric field leads to an overall increase in the momentum spread, in both calculations, it is clear that the standard deviation in p_y increases monotonically for OAM values in the range $\ell = 0$ to $\ell = 8$ and the conclusions are unaffected. Therefore, if the laser OAM magnitudes were unknown prior to conducting an experiment under this scheme, assuming all other laser parameters are held constant, one could distinguish these different OAM states of light.
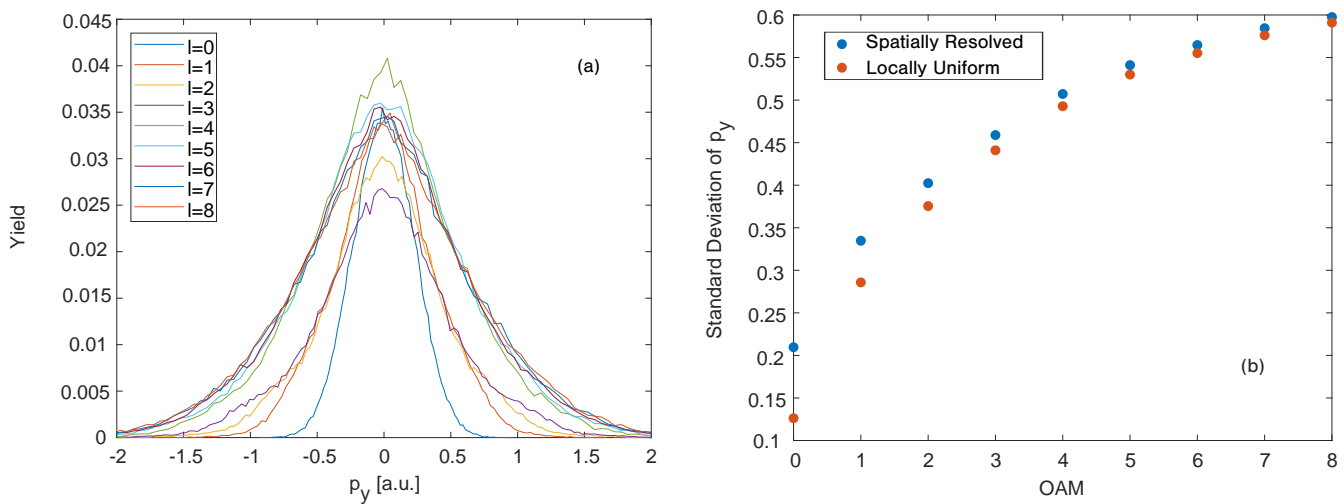

Figure 7. Results of CTMC calculations with the terahertz field included. (**a**) Distribution of ionized photo-electrons in the $\hat{\mathbf{y}}$−direction parallel to the THz field polarization determined using Equation (12) for pumping LG beams containing OAM $\ell = 0, \cdots, 8$. (**b**) Standard deviation values corresponding to the momentum distribution from panel (**a**). Blue points correspond to the data shown in panel (**a**). Red points correspond to an additional approximation valid for short electron excursion. Fields are held constant (in space) at the coordinate of parent ions and momenta are determined from Equation (6). 10^5 trajectories are sampled for each value of ℓ.

The range of OAM states one can distinguish using this technique is limited by the size of the vortex ring (Equation (3)) with respect to the terahertz wavelength. If r_{peak} exceeds one quarter of the terahertz wavelength, i.e.,

$$\frac{\lambda_{\text{THz}}}{4} \lesssim w_0 \sqrt{\frac{|\ell|}{2}}, \tag{13}$$

then the terahertz field is no longer monotonically increasing or decreasing within the range of the momentum ring, as is seen in Figure 3. That is, there is no longer a one-to-one correspondence between the ionization location along $\hat{\mathbf{x}}$ and terahertz electric field value. This leads to a saturation in the in the p_y standard deviation, making it impossible to distinguish OAM values satisfying the above inequality. For the specific beam parameters chosen here, the cutoff occurs at $\ell = 8$. Based on the inequality (13), more OAM states can be distinguished by either increasing λ_{THz} or decreasing the vortex beam waist radius w_0. As the OAM exceeds $\ell = 8$, the standard deviation in p_y will remain around the peak

value and then begin to decrease. The full photo-electron $\hat{y}$ momentum distributions are shown in panel (a) for the accurate spatially resolved case and further affirm these ideas. Photo-electron momentum distributions become nearly indistinguishable as ℓ approaches this cutoff value.

4. Discussion

Having introduced this new technique for distinguishing OAM states, it is worthwhile comparing and contrasting it to that of reference [36] which inspired this work. As stated in the introduction, this proposed scheme and the two-color co-rotating setup [36] share the benefit of being non-destructive to the pulse under investigation. However, unlike the co-rotating method, this one does not require beam sculpting and instead requires the implementation of a terahertz standing wave. That stated, the co-rotating technique maintains the advantage of being able to distinguish positive and negative ℓ values, whereas our proposed scheme can only distinguish between different magnitudes $|\ell|$. Overall, the applicability of one method over another depends most on the needs and physical constraints of the experiment at hand.

While the present work employed a linearly polarized probe pulse to be characterized, we believe this classification scheme can be extended to arbitrary ellipticities. As is discussed in the Results and visualized within Figure 3, this technique's applicability is limited only by the vortex field intensity profile, not its polarization. As long as the probe pulse $\mathbf{E}_{\text{THz}}$ remains polarized along $\hat{y}$ with a node centered at the origin, it will impart additional variation in the photo-electrons' y-momentum. The analysis is complicated by the fact that photo-electrons generated from elliptical pulses display more complicated momentum distributions [42] which must be studied using elliptical integration [43]. However, we expect the underlying mechanism of imparting additional y-momentum via the terahertz pulse to be the same.

The intensity method is intended to characterize a general class of structured fields and is not restricted to the current application of LG beams. As long as applied THz fields have a non-zero component perpendicular to the tunnel exit and a field gradient parallel to the THz propagation direction, a version of the method should be applicable. The standing THz field in our application propagates along the x-axis and is polarized along the y-axis. This means that atoms located along the LG intensity ring of radius r_{peak} experience a different THz field intensity depending on the x-component of their atomic coordinate. This coordinate is parallel to the THz propagation direction. The atomic locations x are bounded between $-r_{\text{peak}}$ and r_{peak} in the current vortex-centered co-ordinate system. This means that one should be able to determine the location of a single ionized atom from features imprinted on the transverse momentum distribution. The only condition is that each atomic position must be assigned a single monotonically increasing intensity value. The exact form of this map depends on both microscopic properties of ionization and the intensity distribution of fields to be characterized. The exact analytic form of this map is as of yet unknown. In a particular experiment one should pre-compute transverse momentum distributions for different field values $|\ell|$ and determine the OAM of fields from comparisons of experimental measurements with these pre-determined reference values.

The situation changes when a distribution of atoms are ionized over the vortex beam. Assuming a uniform gas density and an intensity profile with reflection symmetry across the y-z plane for $x = 0$ we are free to require only that the intensity is single valued in $|x|$. This detail means that the range of $|x|$ spans from 0 to r_{peak} and that the method may be applied to determine larger OAM values $|\ell|$. Microscopic momentum distributions are macroscopically averaged to determine a single transverse distribution over atoms with an $|x|-$coordinate in the entire interval $[0, r_{\text{peak}}]$. The probing THz field essentially acts as a "diffraction" grating. Atoms ionized near the zero-point of the THz field have essentially the same photo-electron momentum distribution as atoms ionized by a LG field alone. If one looks instead at atoms ionized at an atomic location where the THz field is non-zero the story becomes different. When ionization happens at atomic locations corresponding to

non-zero values of the THz field, photo-electron distributions from an individual atom are modified. Photo-electron momentum features transverse to the tunnel exit are broadened (the standard deviation of p_y increases). Since features due to largest values of $|x|$ broaden the transverse distribution most and $r_{\text{peak}} \sim \sqrt{|\ell|}$ we are able to determine the value of $|\ell|$ from the transverse distribution.

Additionally, the polarization vector associated with the THz field does not need to be perfectly perpendicular to the polarization vector of the LG field to be characterized. As long as the two fields have a non-zero offset angle the method should be applicable, but higher THz intensities may be required since we care most about the field component transverse to the tunnel exit.

If the THz probing pulse polarization remains perpendicular to the LG polarization vector, but has a non-zero momentum component along the $z-$axis, then the method will be applicable, but breakdown of the single-valuedness condition set by Equation (13) is modified and becomes

$$\frac{\lambda_{\text{THz}}}{4} \cos \Delta \lesssim w_0 \sqrt{\frac{|\ell|}{2}}, \tag{14}$$

where Δ defines the angle between the THz field's propagation direction and the x-y plane ($\Delta = 0$ for our calculations). This trigonometric term is important. As Δ increases, the component of the displacement vector described by a single THz field wavelength along the x-axis reduces by the trigonometric factor $\cos \Delta$. Once $\Delta \to \pi/2$, the transverse momentum distribution will only contain information about atomic locations along the $z-$axis.

Similarly, we speculate that for THz propagation vectors within the x-y plane but with polarization vector not perfectly orthogonal to the LG polarization, the method is still applicable. Our LG fields contain a single ℓ value and therefore have cylindrically symmetric intensity rings. This means that any THz propagation directions within the x-y plane are sensing the same atomic locations between 0 and r_{peak}, but now over the new field propagation axis $\cos \delta \, \hat{\mathbf{x}} + \sin \delta \, \hat{\mathbf{y}}$ ($\delta = 0$ in our current investigation). When $\delta \to \pi/2$, the THz field has no component parallel to the tunnel exit and the method will fail. Stronger THz intensities are required to broaden the p_y distribution for $\delta \neq 0$.

Understanding how individual microscopic atomic contributions are averaged over the macroscopic gas density allows us to extract the length scale r_{peak} associated with the LG ring of intensity. This is purely an intensity measurement and independent of the OAM phase factor $e^{i\ell\phi}$ itself. We care only that the radius associated with the ring of intensity r_{peak} increases with $|\ell|$. This means that we are unable to determine the sign of ℓ, but the THz field method may be applied to determine length-scales associated with intensity distributions belonging to other forms of structured light. We only care that the THz intensity is weak enough to not ionize on its own and strong enough to cause broadening in the transverse momentum distribution. Otherwise one is able to determine length scales associated with beam features parallel to the THz propagation direction. If fields lack this reflection symmetry, then other moments of the transverse distribution should be analyzed as well.

The relatively simple ionization model applied in the current work is intended to show that THz fields modify trajectories of ionized electrons in such a way that field OAM may be determined. More detailed ionization models may describe a modified (unbroadened) transverse momentum distribution, but broadening by the THz field will happen in exactly the same way. Transverse momentum distributions may be applied to determine length-scales parallel to the THz field propagation.

Further work should be performed to investigate the moments of the transverse momentum distribution. Exactly what is the monotonic map between the locations of ionized atoms and the standard deviation of the transverse momentum distribution? Additionally, can higher moments tell us more about locations of ionized atoms? It is clear that THz fields are able to imprint distance information onto transverse distributions. How

can one characterize other dimensions of the field? It is clear that THz fields are useful tools to determine spatial properties of structured light, but additional investigations must determine to what degree.

5. Conclusions

We have proposed a method for determining the magnitude of OAM, ℓ, contained within linearly-polarized LG beams using an additional terahertz probing field propagating perpendicular to the aforementioned LG beam. When the terahertz probe is turned off, strong field ionization by Laguerre–Gaussian light beams leads to local carrier envelope phase effects in the photo-electron momentum distributions associated with the electron's ionization location. When focal averaging is performed, the presence of these local CEP effects allow us to distinguish between vortex and non-vortex beams with circular polarization. By turning on the terahertz beam, photo-electrons achieve additional variation in their y-momentum which can be mapped to the size of the vortex ring, and therefore the magnitude of the OAM index $|\ell|$. Unlike many previous techniques, the method is nondestructive and does not require additional beam sculpting. Through the comparison of experimental results with Monte Carlo simulations, the unknown ℓ value can be obtained solely from the velocity distribution of measured photo-electrons transverse to the tunnel exit. It is clear that THz fields are useful tools to determine length-scales associated with photo-ionization.

Author Contributions: H.P. came up with the set-up and performed the simulations. H.P., A.S. and S.W. wrote the initial draft. A.S.L. supervised the project and edited the draft. All authors contributed to the project, discussed the results and assisted with draft preparation. All authors have read and agreed to the published version of the manuscript.

Institutional Review Board Statement: Not applicable.

Informed Consent Statement: Not applicable.

Data Availability Statement: Simulation data can be made available upon reasonable request.

Conflicts of Interest: The authors declare no conflict of interest.

Abbreviations

The following abbreviations are used in this manuscript:

ADK	Ammosov–Delone–Krainov (Ref. [38])
CEP	carrier envelope phase
CTMC	classical trajectory Monte Carlo
LG	Laguerre–Gaussian
OAM	orbital angular momentum
SAM	spin angular momentum
SFI	strong field ionization
TIPIS	tunnel ionization in parabolic coordinates with induced dipole and Stark shift

References

1. Berestetskii, V.; Lifshitz, E.; Pitaevskii, L. *Quantum Electrodynamics*; Elsevier: Amsterdam, The Netherlands, 1982.
2. Jackson, J.D. *Classical Electrodynamics*; John Wiley & Sons: Hoboken, NJ, USA, 2021.
3. Allen, L.; Beijersbergen, M.W.; Spreeuw, R.J.C.; Woerdman, J.P. Orbital angular momentum of light and the transformation of Laguerre–Gaussian laser modes. *Phys. Rev. A* **1992**, *45*, 8185–8189. [CrossRef] [PubMed]
4. Dubois, J.; Lévêque, C.; Caillat, J.; Taïeb, R.; Saalmann, U.; Rost, J.M. Strong-field photoionization by circularly polarized light. *arXiv* **2023**, arXiv:2306.12999.
5. Walker, S.; Kolanz, L.; Venzke, J.; Becker, A. Selectivity in electron emission induced by ultrashort circularly polarized laser pulses. *Phys. Rev. Res.* **2021**, *3*, 043051. [CrossRef]

6. Colton, D.L.; Kress, R. *Inverse Acoustic and Electromagnetic Scattering Theory*; Springer: Berlin/Heidelberg, Germany, 1998; Volume 93. [CrossRef]
7. Matula, O.; Hayrapetyan, A.G.; Serbo, V.G.; Surzhykov, A.; Fritzsche, S. Atomic ionization of hydrogen-like ions by twisted photons: Angular distribution of emitted electrons. *J. Phys. B At. Mol. Opt. Phys.* **2013**, *46*, 205002. [CrossRef]
8. Brambilla, M.; Battipede, F.; Lugiato, L.A.; Penna, V.; Prati, F.; Tamm, C.; Weiss, C.O. Transverse laser patterns. I. Phase singularity crystals. *Phys. Rev. A* **1991**, *43*, 5090–5113. [CrossRef] [PubMed]
9. Bazhenov, V.Y.; Soskin, M.; Vasnetsov, M. Screw dislocations in light wavefronts. *J. Mod. Opt.* **1992**, *39*, 985–990. [CrossRef]
10. Shen, Y.; Wang, X.; Xie, Z.; Min, C.; Fu, X.; Liu, Q.; Gong, M.; Yuan, X. Optical vortices 30 years on: OAM manipulation from topological charge to multiple singularities. *Light. Sci. Appl.* **2019**, *8*, 90. [CrossRef]
11. Coullet, P.; Gil, L.; Rocca, F. Optical vortices. *Opt. Commun.* **1989**, *73*, 403–408. [CrossRef]
12. Mair, A.; Vaziri, A.; Weihs, G.; Zeilinger, A. Entanglement of the orbital angular momentum states of photons. *Nature* **2001**, *412*, 313–316. [CrossRef]
13. Berkhout, G.C.G.; Beijersbergen, M.W. Method for Probing the Orbital Angular Momentum of Optical Vortices in Electromagnetic Waves from Astronomical Objects. *Phys. Rev. Lett.* **2008**, *101*, 100801. [CrossRef]
14. Harwit, M. Photon orbital angular momentum in astrophysics. *Astrophys. J.* **2003**, *597*, 1266. [CrossRef]
15. Tamburini, F.; Thidé, B.; Molina-Terriza, G.; Anzolin, G. Twisting of light around rotating black holes. *Nat. Phys.* **2011**, *7*, 195–197. [CrossRef]
16. Jeffries, G.D.; Edgar, J.S.; Zhao, Y.; Shelby, J.P.; Fong, C.; Chiu, D.T. Using polarization-shaped optical vortex traps for single-cell nanosurgery. *Nano Lett.* **2007**, *7*, 415–420. [CrossRef] [PubMed]
17. Yang, Y.; Wu, Y.; Zheng, X.; Shi, J.; Luo, Y.; Huang, J.; Deng, D. Particle manipulation with twisted circle Pearcey vortex beams. *Opt. Lett.* **2023**, *48*, 3535–3538. [CrossRef] [PubMed]
18. Wang, T.; Ke, M.; Li, W.; Yang, Q.; Qiu, C.; Liu, Z. Particle manipulation with acoustic vortex beam induced by a brass plate with spiral shape structure. *Appl. Phys. Lett.* **2016**, *109*, 123506. [CrossRef]
19. Gibson, G.; Courtial, J.; Padgett, M.J.; Vasnetsov, M.; Pas'ko, V.; Barnett, S.M.; Franke-Arnold, S. Free-space information transfer using light beams carrying orbital angular momentum. *Opt. Express* **2004**, *12*, 5448–5456. [CrossRef] [PubMed]
20. Wang, J.; Yang, J.Y.; Fazal, I.M.; Ahmed, N.; Yan, Y.; Huang, H.; Ren, Y.; Yue, Y.; Dolinar, S.; Tur, M.; et al. Terabit free-space data transmission employing orbital angular momentum multiplexing. *Nat. Photonics* **2012**, *6*, 488–496. [CrossRef]
21. Schmiegelow, C.T.; Schulz, J.; Kaufmann, H.; Ruster, T.; Poschinger, U.G.; Schmidt-Kaler, F. Transfer of optical orbital angular momentum to a bound electron. *Nat. Commun.* **2016**, *7*, 12998. [CrossRef]
22. Picón, A.; Mompart, J.; de Aldana, J.V.; Plaja, L.; Calvo, G.; Roso, L. Photoionization with orbital angular momentum beams. *Opt. Express* **2010**, *18*, 3660–3671. [CrossRef]
23. Picón, A.; Benseny, A.; Mompart, J.; de Aldana, J.V.; Plaja, L.; Calvo, G.F.; Roso, L. Transferring orbital and spin angular momenta of light to atoms. *New J. Phys.* **2010**, *12*, 083053. [CrossRef]
24. Takahashi, H.T.; Proskurin, I.; Kishine, J.i. Landau Level Spectroscopy by Optical Vortex Beam. *J. Phys. Soc. Jpn.* **2018**, *87*, 113703 . [CrossRef]
25. Zürch, M.; Kern, C.; Hansinger, P.; Dreischuh, A.; Spielmann, C. Strong-field physics with singular light beams. *Nat. Phys.* **2012**, *8*, 743–746. [CrossRef]
26. Patchkovskii, S.; Spanner, M. High harmonics with a twist. *Nat. Phys.* **2012**, *8*, 707–708. [CrossRef]
27. Dorney, K.M.; Rego, L.; Brooks, N.J.; San Román, J.; Liao, C.T.; Ellis, J.L.; Zusin, D.; Gentry, C.; Nguyen, Q.L.; Shaw, J.M.; et al. Controlling the polarization and vortex charge of attosecond high-harmonic beams via simultaneous spin–orbit momentum conservation. *Nat. Photonics* **2019**, *13*, 123–130. [CrossRef]
28. Rego, L.; Dorney, K.M.; Brooks, N.J.; Nguyen, Q.L.; Liao, C.T.; San Román, J.; Couch, D.E.; Liu, A.; Pisanty, E.; Lewenstein, M.; et al. Generation of extreme-ultraviolet beams with time-varying orbital angular momentum. *Science* **2019**, *364*, eaaw9486. [CrossRef] [PubMed]
29. Hernández-García, C.; Picón, A.; San Román, J.; Plaja, L. Attosecond Extreme Ultraviolet Vortices from High-Order Harmonic Generation. *Phys. Rev. Lett.* **2013**, *111*, 083602. [CrossRef] [PubMed]
30. Vieira, J.; Trines, R.M.G.M.; Alves, E.P.; Fonseca, R.A.; Mendonça, J.T.; Bingham, R.; Norreys, P.; Silva, L.O. High Orbital Angular Momentum Harmonic Generation. *Phys. Rev. Lett.* **2016**, *117*, 265001. [CrossRef]
31. Sen, A.; Sinha, A.; Sen, S.; Sharma, V.; Gopal, R. Above-threshold ionization of argon with ultrashort orbital-angular-momentum beams. *Phys. Rev. A* **2022**, *106*, 023103. [CrossRef]
32. Paufler, W.; Böning, B.; Fritzsche, S. Strong-field ionization with twisted laser pulses. *Phys. Rev. A* **2018**, *97*, 043418. [CrossRef]
33. Leach, J.; Padgett, M.J.; Barnett, S.M.; Franke-Arnold, S.; Courtial, J. Measuring the Orbital Angular Momentum of a Single Photon. *Phys. Rev. Lett.* **2002**, *88*, 257901. [CrossRef]
34. Yu, B.S.; Li, C.Y.; Yang, Y.; Rosales-Guzmán, C.; Zhu, Z.H. Directly Determining Orbital Angular Momentum of Ultrashort Laguerre–Gauss Pulses via Spatially-Resolved Autocorrelation Measurement. *Laser Photonics Rev.* **2022**, *16*, 2200260. [CrossRef]
35. Hickmann, J.M.; Fonseca, E.J.S.; Soares, W.C.; Chávez-Cerda, S. Unveiling a Truncated Optical Lattice Associated with a Triangular Aperture Using Light's Orbital Angular Momentum. *Phys. Rev. Lett.* **2010**, *105*, 053904. [CrossRef] [PubMed]
36. Fang, Y.; Guo, Z.; Ge, P.; Dou, Y.; Deng, Y.; Gong, Q.; Liu, Y. Probing the orbital angular momentum of intense vortex pulses with strong-field ionization. *Light. Sci. Appl.* **2022**, *11*, 34. [CrossRef]

37. Goldsmith, P.F. *Quasioptical Systems: Gaussian Beam Quasioptical Propogation and Applications*; Wiley-IEEE Press: Hoboken, NJ, USA, 1998; pp. 9–38. [CrossRef]

38. Ammosov, M.V.; Delone, N.B.; Krainov, V.P. Tunnel ionization of complex atoms and of atomic ions in an alternating electromagnetic field. *Sov. J. Exp. Theor. Phys.* **1986**, *64*, 1191.

39. Ortmann, L.; Pérez-Hernández, J.A.; Ciappina, M.F.; Schötz, J.; Chacón, A.; Zeraouli, G.; Kling, M.F.; Roso, L.; Lewenstein, M.; Landsman, A.S. Emergence of a Higher Energy Structure in Strong Field Ionization with Inhomogeneous Electric Fields. *Phys. Rev. Lett.* **2017**, *119*, 053204. [CrossRef] [PubMed]

40. Vicario, C.; Monoszlai, B.; Hauri, C.P. GV/m Single-Cycle Terahertz Fields from a Laser-Driven Large-Size Partitioned Organic Crystal. *Phys. Rev. Lett.* **2014**, *112*, 213901. [CrossRef]

41. Pfeiffer, A.N.; Cirelli, C.; Smolarski, M.; Dimitrovski, D.; Abu-Samha, M.; Madsen, L.B.; Keller, U. Attoclock reveals natural coordinates of the laser-induced tunnelling current flow in atoms. *Nat. Phys.* **2012**, *8*, 76–80. [CrossRef]

42. Mur, V.; Popruzhenko, S.; Popov, V. Energy and momentum spectra of photo-electrons under conditions of ionization by strong laser radiation (The case of elliptic polarization). *J. Exp. Theor. Phys.* **2001**, *92*, 777–788. [CrossRef]

43. Hofmann, C.; Landsman, A.S.; Cirelli, C.; Pfeiffer, A.N.; Keller, U. Comparison of different approaches to the longitudinal momentum spread after tunnel ionization. *J. Phys. B At. Mol. Opt. Phys.* **2013**, *46*, 125601. [CrossRef]